

Determination of glucose flux in live myoblasts by microfluidic nanosensing and mathematical modeling

*Original*

Determination of glucose flux in live myoblasts by microfluidic nanosensing and mathematical modeling / Zambon, A.; Zoso, A.; Luni, C.; Frommer, W. B.; Elvassore, N.. - In: INTEGRATIVE BIOLOGY. - ISSN 1757-9694. - ELETTRONICO. - 6:3(2014), pp. 277-288. [10.1039/c3ib40204e]

*Availability:*

This version is available at: 11583/2785699 since: 2020-02-12T14:54:58Z

*Publisher:*

Royal Society of Chemistry

*Published*

DOI:10.1039/c3ib40204e

*Terms of use:*

This article is made available under terms and conditions as specified in the corresponding bibliographic description in the repository

*Publisher copyright*

(Article begins on next page)

# Determination of glucose flux in live myoblasts by microfluidic nanosensing and mathematical modeling

*Alessandro Zambon<sup>†a,b</sup>, Alice Zoso<sup>†a,b</sup>, Camilla Luni<sup>a,b</sup>, Wolf B. Frommer<sup>c</sup> and  
Nicola Elvassore<sup>\*a,b</sup>*

<sup>a</sup> Department of Industrial Engineering, University of Padova, Padova, Italy.

<sup>b</sup> Venetian Institute of Molecular Medicine (VIMM), Padova, Italy.

<sup>c</sup> Department of Plant Biology, Carnegie Institution for Science, Stanford, CA, USA

\* Author to whom correspondence should be addressed.

E-mail: nicola.elvassore@unipd.it; Fax: +39 049 827-5461; Tel: +39 049 827-5469

† These authors contributed equally to this work.

*Integrative Biology*  
In press  
DOI: 10.1039/c3ib40204e

## **Abstract**

Glucose is the main energy source for cells in an organism and its blood concentration is tightly regulated in healthy individuals. However, impaired blood glucose control has been found in diseases such as metabolic syndrome and diabetes, and anomalous glucose utilization in cancer tissues. Dissecting the dynamics of the different phenomena involved in glucose handling (intracellular mass transport, membrane diffusion, and intracellular phosphorylation) is very relevant to identify which mechanisms are disrupted under disease conditions. In this work, we developed an effective methodology for quantitatively analyzing these phenomena in living cells. A measurement of steady-state glucose uptake is, by itself, insufficient to determine the dynamics of intracellular glucose. For this purpose, we integrated two types of measurements: cytosolic glucose concentration at the single-cell level, obtained using a cytosolic FRET nanosensor, and cell population glucose uptake, obtained without perturbing culture conditions using a microfluidic perfusion system. Microfluidics enabled accurate temporal stimulation of cells through cyclic pulses of glucose concentration at defined flow rates. We found that both, glucose uptake and phosphorylation, are linearly dependent on glucose concentration in the physiologic range. Mathematical modeling enabled precise determination of the kinetic constants of membrane transport ( $0.27 \text{ s}^{-1}$ ) and intracellular phosphorylation ( $2.01 \text{ s}^{-1}$ ).

## **Insight, innovation, integration**

Quantitatively studying cellular glucose handling is very relevant for better understanding alterations implicated in diseases, like diabetes and cancer. Although of critical importance, an investigation of glucose kinetics under physiological conditions is still lacking. Here, we performed a quantitative dissection of the mechanisms that involve glucose uptake and metabolism in a culture of cells from skeletal muscle, one of the primary tissues responsible for glucose uptake in the body. We accurately controlled the extracellular microenvironment performing experiments within a microfluidic culture system. Data were analyzed through a mathematical model for quantification. Combining experimental technology and modeling enabled precise determination of rates of glucose diffusion across cell membrane and intracellular phosphorylation, and their dependence on external glucose concentration under physiologic conditions and under perturbation.

## Introduction

Glucose is the primary energy source for cells in an organism and its blood concentration is tightly regulated in healthy individuals (3.9-6.1 mmol/L)<sup>1,2</sup>. Impaired blood glucose control has been found in diseases such as metabolic syndrome and diabetes, with serious consequences for patients<sup>3,4</sup>. Furthermore, alterations in glucose flux has been implicated in cancer development through the so-called Warburg effect<sup>5</sup>.

In a cell culture there are three different phenomena involved in glucose handling: intracellular mass transport, diffusion through plasma membrane, and intracellular phosphorylation. Dissecting their dynamics is very important for identifying compromised mechanisms at the single-cell level relevant for disease conditions.

Intracellular mass transport represents the movement of glucose in the culture medium by diffusion and, in case of a perfused system, also by convection. This process is dependent on the geometry and operative conditions of the experimental setup used, however computational modeling can easily describe the glucose concentration field in different systems by solving its microscopic mass balance, coupled with fluid dynamic simulations in case of perfused systems<sup>6</sup>.

Diffusion through plasma membrane brings intracellular glucose into the cells through glucose transporters (GLUTs, SGLTs and SWEETs). Multiple GLUT isoforms have been discovered whose membrane expression is highly regulated<sup>7</sup>, either through hormonal control (for example, by insulin) or by intracellular mechanisms such as glycosylation<sup>8,9</sup>. Glucose transport across the cell membrane is conventionally studied *in vitro* using glucose analogs. The most commonly used are radioactive hexoses, such as [<sup>14</sup>C] 2-deoxy-D-glucose<sup>10</sup> and [<sup>18</sup>F] fluoro-2-deoxy-D-glucose<sup>11</sup>. Besides the criticality of working with radioactivity, radiolabeled analogs present some limitations, such as lack of spatio-temporal resolution and the inability to measure glucose uptake in viable cell cultures<sup>12</sup>. To avoid these shortcomings, non-metabolizable and metabolizable fluorescence-tagged glucose analogs were developed, the most common being 6- and 2-(N-(7-Nitrobenz-2-oxa-1,3-diazol-4-yl)amino)-6-Deoxyglucose (6-NBDG and 2-NBDG)<sup>13,14</sup>. Compared to radioisotopes fluorescently labeled analogs provide high spatial and temporal resolution, with fluorescence detectable at the single cell level within seconds<sup>12</sup>. However, a common limitation to both isotope and fluorescent analogs is that they are not transported by GLUTs and metabolized by hexokinase with the same kinetics as glucose<sup>12</sup>, and they can be toxic

even at low doses<sup>15</sup>. More recently nanosensors were developed for intracellular glucose imaging in live cells at single-cell resolution<sup>16</sup>. They are based on the interaction of intracellular D-glucose with a molecular probe that, upon glucose binding, undergoes a conformational rearrangement detectable by Förster resonance energy transfer (FRET) between two spectral GFP variants. FRET is a direct proxy for the cytosolic glucose concentration at steady state<sup>17</sup>. While non-steady-state FRET changes can be correlated to changes in cytosolic glucose concentration only if the nanosensor kinetics is faster than that of intracellular glucose processes. If this condition is not met, a dynamic use of the nanosensor is precluded.

After import into the cell, glucose is phosphorylated by hexokinases. Multiple isoforms of this enzyme exist in different tissues<sup>18</sup>. Hexokinase kinetics has been studied after enzyme purification mainly by spectrophotometric techniques<sup>19,20,21</sup>. One study measured hexokinase rate of glucose phosphorylation within the complexity of cytoplasmic environment<sup>22</sup>. However, in this study nanosensor kinetics is assumed to be faster than hexokinase rate.

A comprehensive investigation to simultaneously dissect intracellular glucose transport, its diffusion through plasma membrane, and its intracellular phosphorylation in a quantitative manner is still missing. These three processes occur sequentially, and at steady-state their rates are the same and equal to the rate of the slowest of the three steps. Thus, measuring the uptake of glucose by cells at steady-state gives information on the overall speed of the process, but does not allow the identification of the dynamics of each of the three steps individually. A deeper study is needed for a quantitative analysis of these processes and of the impairments occurring in pathological conditions.

Here, we performed a dissection of the dynamics of the three processes involved in glucose acquisition in a myoblast cell culture. We took advantage of different experimental and computational techniques for the study of mass transport and myoblast kinetics of glucose uptake and phosphorylation. We coupled the detection of cytosolic glucose concentration via FRET-based nanosensors at the single-cell level with the enzymatic measurement of glucose uptake of a cell population, performed with minimal culture perturbation. We performed the experiments within a microfluidic culture system to accurately control the extracellular environment and in particular glucose concentration in the immediate vicinity of cell membrane. The small volumes of medium used also increased the signal-to-noise

ratio of measurements because a small glucose uptake by the cells produced a large concentration difference in the culture medium. Experimental data were analyzed making use of mathematical modeling to derive the kinetic constants of each glucose-related process.

## **Results and discussion**

### **Experimental strategy**

Dissecting the dynamics of glucose intracellular mass transport, diffusion through plasma membrane, and intracellular phosphorylation in a quantitative manner is not feasible by measuring steady-state glucose uptake or glucose intracellular concentration alone<sup>22</sup>. A more thorough analysis is needed to characterize each of these processes. We used mathematical modeling to theoretically determine which measurements are required to quantify each rate. The model we developed is multi-scale and describes the glucose concentration field in the whole culture system, the cell population glucose uptake and the single-cell processes of glucose handling. It is based on standard techniques of fluid dynamic modeling and glucose mass balances. We found that, by coupling the two measurements of steady-state glucose uptake and cytosolic glucose concentration, it is possible to fully quantify the kinetics of each of the three processes involved in glucose handling.

Based on this theoretical result, we set up a microfluidic experimental system for accurately performing the two measurements, steady-state glucose uptake and cytosolic glucose concentration (Figure 1). The microfluidic chip allowed a tight control of glucose concentration thanks to the perfusion in laminar flow conditions and an accurate temporal stimulation of the cells obtained by coupling the chip with an automated liquid handling apparatus. Each chip included three culture chambers to perform experiments in triplicate and was made of transparent PDMS to perform fluorescence microscopy on line.

To determine the overall glucose uptake in each cell culture chamber, we carried out steady-state experiments at defined inlet glucose concentrations and measured glucose concentration at the outlet (Figure 2). Uptake was then calculated from the overall mass balance on the culture system (Eq. (9)). Thanks to the low flow rates used (12.5 nL/min) and the very high surface-to-volume ratio of the culture chamber (Table I), the difference of glucose concentration between inlet and outlet had a significant signal-to-noise ratio, because a small flux of glucose into the cells resulted in a large concentration variation in

the culture medium.

To obtain the second type of measurement, cytosolic glucose concentration in individual cells, the response of the intracellular FRET-based nanosensor FLIPglu-600 $\mu\Delta$ 13V<sup>17</sup> was detected online by microscopy (Figure 3). A high flow rate (4  $\mu$ L/min) was used in these experiments in order to have a glucose concentration on the cell surface approximately equal to its concentration at the inlet of the culture system, i.e. the glucose assimilated by cells was negligible compared to the amount of glucose entering the system. These measurements were taken both at steady state and under fast dynamic changes of inlet glucose concentration. We used a multi-inlet system to switch between different glucose concentrations entering the culture chamber with high temporal accuracy by means of pneumatic valves integrated on chip (Figure 1). For example it can be easily used to generate a pulse or an approximately linear ramp of concentrations.

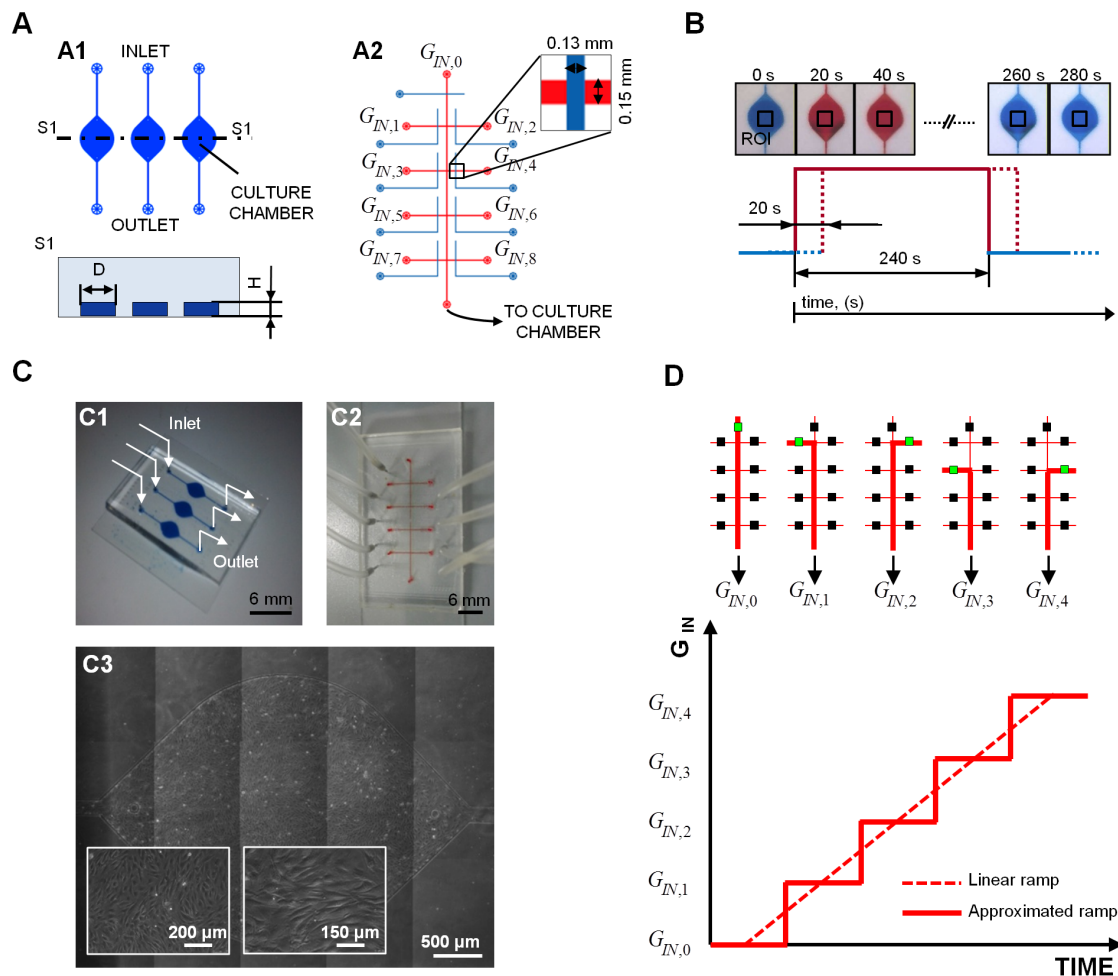


**Figure 1.** Experimental setup. (A) A1) Top view and section of the microfluidic cell culture chambers. A2) Top view of the multi-inlet system for FRET experiments. Blue lines: microfluidic channels used to pneumatically control the valve system. Red lines: flow channels connecting external medium reservoirs at different glucose concentrations ( $G_{IN,i}$  with  $i = 1 \dots 9$ ) to the inlet of a culture chamber. Enlargement shows the detail of a pneumatic valve. (B) Analysis of the delay between a change in input conditions and the actual change of medium composition in the culture chamber, using dyes of different colors, at 4- $\mu$ L/min flow rate. ROI: region of interest. (C) C1) and C2) Pictures of the experimental setup schematically represented in A). The culture chambers and the flow channels in the multi-inlet system were filled with blue and red dyes, respectively. C3) Images of the culture chamber after seeding of myoblasts, at different enlargements. (D) Example of the functionality of the multi-inlet system for reproducing an approximately linear ramp of glucose concentration at the inlet of the culture chamber. In the upper part, the system is schematically depicted with green and black squares representing open and closed valves, respectively.

## Validation of glucose uptake measurements

We verified the sensitivity of our system for glucose uptake measurements and optimized parameters for imaging and perfusion. Myoblasts were seeded within the microfluidic chambers and perfusion started after cell adhesion. We studied how sensitive the measurements of glucose concentration at the outlet of the culture chamber were to different flow-rate regimes. As flow rate is inversely correlated to the residence time of medium in the culture chamber, we expected the measurements to be less sensitive at high flow rates when glucose outlet concentration was expected not to be significantly different from the inlet concentration.

First, we applied a step change in flow rate from 0.025 to 0.5  $\mu\text{L}/\text{min}$ , collected the medium continuously at the outlet of the culture chambers, and analyzed it enzymatically every 0.6- $\mu\text{L}$  volume eluted (Figure 2B). Results showed high accuracy: average data variability was approximately 30% both for samples from different culture chambers and for samples collected at different time points at steady-state. At the low flow rate, glucose concentration at the outlet was significantly different from that of the control, represented by a culture chamber where no cells were seeded. On the contrary, at 0.5  $\mu\text{L}/\text{min}$  the steady-state outlet concentration was approximately the same as for the control, and the signal-to-noise ratio too small for an accurate derivation of the uptake rate.

As the time needed to collect a 0.6- $\mu\text{L}$  sample is inversely proportional to the flow rate (Figure 2B, inset), then flow rate also affects the maximum time resolution of the measurement. For example, at 0.025  $\mu\text{L}/\text{min}$  each sampling was performed every 24 min, while at 0.5  $\mu\text{L}/\text{min}$  every 1.2 min. Thus, working at low flow rates increases measurement sensitivity, but at the expenses of time resolution.

From this experiment we also determined the time needed to reach a steady-state condition to be approximately that needed for eluting 2- $\mu\text{L}$  volume (Figure 2B). This result was also confirmed by fluid dynamic simulations (see Supporting Information). In the next steady-state measurements presented, we always collected samples after 3- $\mu\text{L}$  volumes (as an excess of 2  $\mu\text{L}$ ) were eluted following a flow rate change.

To determine the optimal flow rate to use, a second experiment was performed measuring steady-state outlet glucose concentration for six different flow rates ranging between 0.0125 and 0.5  $\mu\text{L}/\text{min}$  (Figure 2C). The experimental results confirmed that the smaller is

the flow rate, the larger is the glucose concentration difference between inlet and outlet, and the higher is glucose uptake measurement sensitivity. However, lower flow rates imply longer times for sample collection and less temporal resolution during dynamic experiments. As a trade-off between these two requirements we decided to perform next experiments of glucose uptake measurement at a flow rate of 0.05  $\mu\text{L}/\text{min}$ .

As single-cell glucose uptake is the measurement usually reported in the literature, we calculated its mean value in the culture chamber as the ratio of the overall uptake, calculated by Eq. (9), to the number of cells in the culture chamber (Figure 2D). For the same inlet glucose concentration and high flow rates, uptake by the average cell was approximately independent from the flow rate. The flow rate can be considered high when glucose gets to cell surface more rapidly than it is consumed. The single-cell uptake we measured ( $\sim 30 \text{ fmol min}^{-1}$  per cell) is of the same order of magnitude of a previous study on myoblasts<sup>23</sup>, where it was obtained from radioactivity measurements after addition of  $^{14}\text{C}(\text{U})$ deoxy-D-glucose. Assuming a total protein content of  $120 \pm 18 \text{ pg/cell}$  (Table I), the uptake from data in Kotliar et al.<sup>23</sup> was  $17 \pm 3 \text{ fmol min}^{-1}$  per cell).

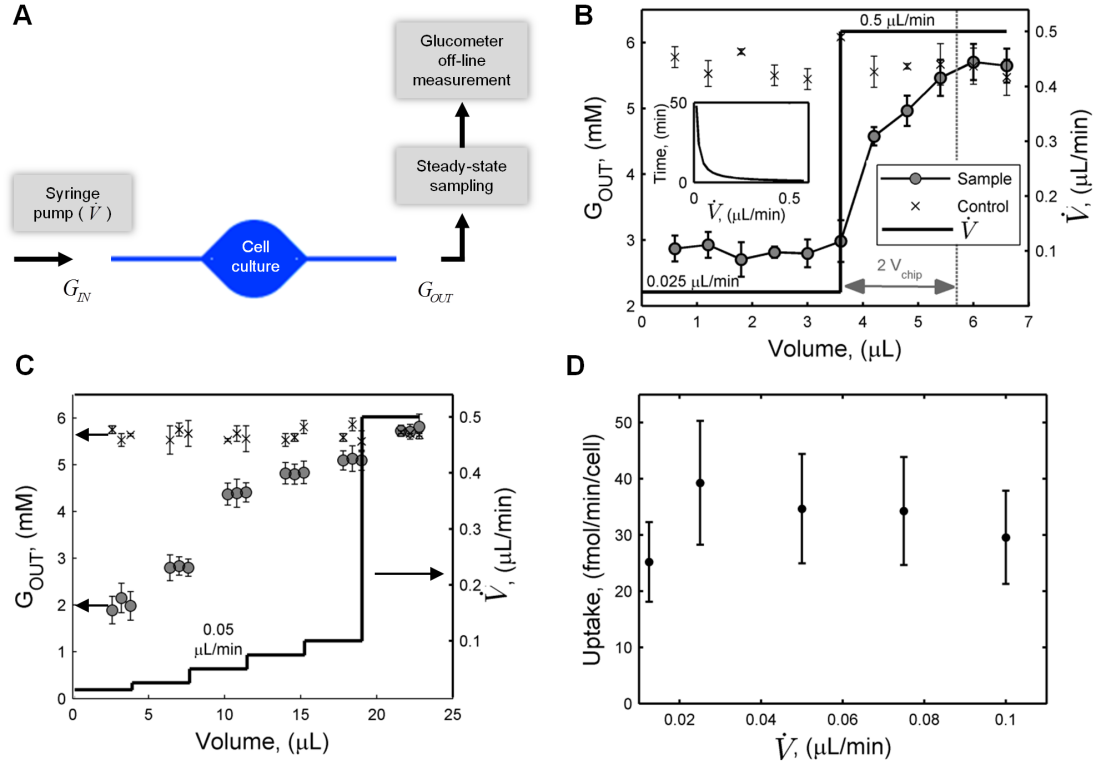


**Figure 2.** Effect of flow rate on glucose uptake measurements. **(A)** Schematic representation of glucose uptake experiments. **(B)** Experimental measurements of outlet glucose concentration after a step change in flow rate as a function of the eluted volume. Sampling was performed continuously (medium was analyzed every 0.6- $\mu\text{L}$  volume eluted). Control data are taken from a chamber having the same inlet conditions as the sample chamber, but no cells inside.  $V_{chip}$  is the total volume, including culture chamber and microfluidic channels (approximately 1  $\mu\text{L}$ ). Error bars represent standard deviation ( $n=3$ ). Inset: computational simulation of the duration of sampling as a function of volumetric flow rate. **(C)** Experimental steady-state measurements of outlet glucose concentration at increasing flow rates, as a function of the eluted volume. Control experiments were performed as in **(B)**. Error bars indicate standard deviation of 3 repeated measurements from the same culture chamber. **(D)** Mean single-cell glucose uptake rate,  $U/N_c$ , in the culture chamber as a function of flow rate, calculated from data in **(C)**.  $G_{IN}$  was equal to  $5.6 \pm 0.3 \text{ mM}$ .

### Validation of dynamic monitoring of cytosolic glucose concentration

We next validated the suitability of our experimental system for cytosolic glucose detection by the FRET-based nanosensor FLIPglu-600 $\mu\Delta$ 13V. Myoblasts were seeded within the microfluidic chamber and transfected with the nanosensor plasmid. We used a high flow rate (4 $\mu\text{L}/\text{min}$ ) in these experiments so that glucose concentration on cell membrane,  $G_m$ ,

was approximately equal to its concentration in the inlet,  $G_{IN}$ . We performed dynamic stimulations of cells alternating glucose-free and 1.5-mM concentration buffer solution, using the multi-inlet system (Figure 3A). Each concentration was kept constant for 4 min during repeated pulses (Figure 3C). Using dyes of different colors, we verified a delay of approximately 20 s between a change of valve opening in the multi-inlet system and the actual change of medium composition in the cell culture chamber, at the flow rate used (Figure 1C). The square-shaped pulse was fairly conserved (Figure 1C).

We performed live cell imaging for FRET detection (Figure 3B), and analyzed the images, as previously reported<sup>17</sup>, to obtain the FRET index  $r$  (Figure 3C). A decrease in this index represents an increase in cytosolic glucose concentration. The results show the accuracy of our measurements, with a consistent return to the FRET index baseline after each stimulation pulse. After 4 min of stimulus, FRET signal approximately reaches a new steady state.

In this work we used FRET results at steady-state to determine cytosolic glucose concentration. For using the nanosensor to determine non-steady-state concentrations, the nanosensor-glucose binding needs to be faster than the other intracellular processes involving glucose (membrane transport, phosphorylation, and maybe others), so that a quasi-steady-state approximation holds and online FRET detection is directly correlated to cytosol glucose concentration. However, we will show later that this condition is not satisfied in our system.

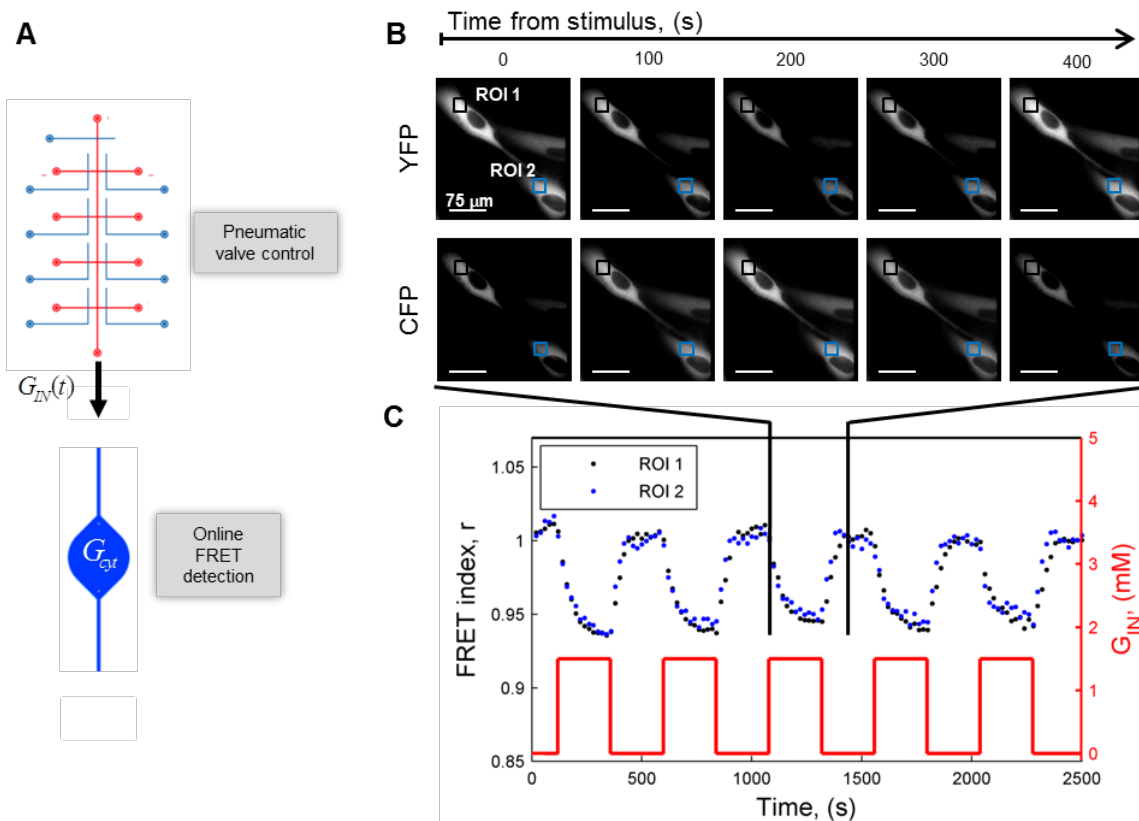


**Figure 3.** Dynamic measurements of intracellular glucose concentration via FRET nanosensor. (A) Schematic representation of FRET experiments. (B) Sequence of images, obtained by fluorescence microscopy, of cyan (CFP) and yellow (YFP) fluorescent signals during pulse perfusion at 1.5 mM glucose concentration. (C) Normalized baseline-corrected FRET index,  $r$ , during an experiment of 4-min cyclic pulses of 1.5-mM glucose concentration. Blue and black dots refer to the two regions of interest (ROIs) shown in A).

### Dissection of myoblast glucose handling mechanisms

We studied how glucose uptake rate changes as a function of extracellular glucose concentration in the physiological range of concentrations (3-13 mM). To this aim, we measured the uptake for different conditions at the inlet of the culture chamber, keeping the flow rate constant and equal to 0.05  $\mu$ L/min. Experimental data showed a linear relationship between inlet and outlet glucose concentration, with the latter being about 74% of the former (Figure 4A).

In order to better understand fluid dynamics and glucose mass transport within the microfluidic chip, we developed a 3-dimensional (3D) mathematical model to simulate the experimental operative conditions. In particular, we aimed at investigating the spatial

heterogeneity within the culture chamber and the actual glucose concentration in the cell microenvironment, i.e. immediately outside of the cell membrane.

The model described glucose uptake as a consumption flux at the bottom of the culture chamber, whose rate was assumed proportional to glucose concentration at this surface. Under this assumption, the numerical simulation reproduced the linearity of the experimental data ( $G_{OUT} = 74\% \cdot G_{IN}$ ), as shown in Figure 4A.

Model results also highlighted that, at the low flow rate used (0.05  $\mu\text{L}/\text{min}$ ), the average glucose concentration outside cell membrane,  $G_m$ , is reduced to 84% of its concentration at the inlet (Figure 4B). However, this result is specific for the setup geometry we used.

By our 3D model we simulated the glucose concentration profile within the culture chamber. As shown in Figure 4C, a cell near the outlet is exposed to a concentration of glucose that is 27% lower compared to a cell located near the inlet. On the other hand, the concentration gradient in the z-direction is very small (Figure 4C and Supporting Information). Thus, spatial heterogeneity is mainly due to the progressive consumption of glucose by cells located upstream during the 14 min taken by medium to convectively flow from inlet to outlet. The measured overall glucose uptake is an average over a spatially heterogeneous cell population. However, as glucose uptake was described as a linear function of concentration, it is reasonable to assume that the overall uptake is the same as if all the cells were exposed to the average of medium composition shown in Figure 4B.

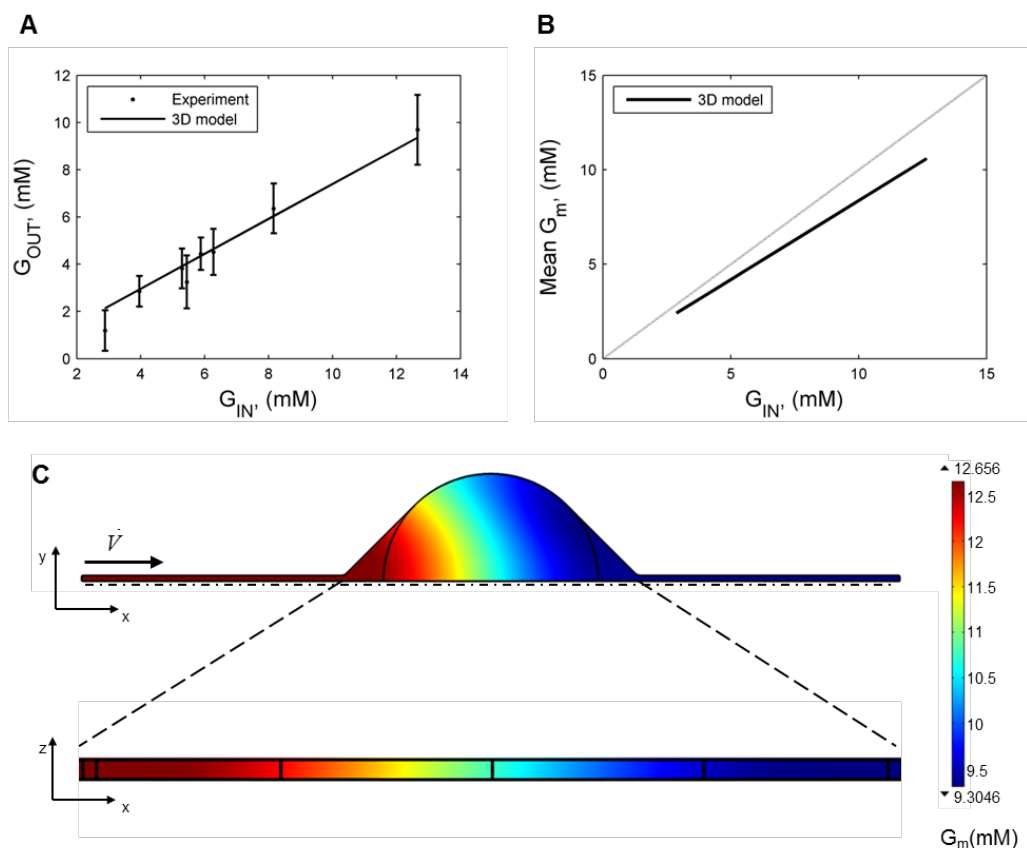


**Figure 4.** Results from glucose uptake experiments and simulations. **(A)** Data of steady-state glucose concentration at the outlet of the culture chamber, obtained from off-line enzymatic measurements, as a function of different inlet glucose concentrations. Error bars: standard deviations ( $n=3$ ). Solid line: results simulated by the 3-dimensional computational model after fitting parameter  $k_U$ . **(B)** Computational estimation of the mean glucose concentration at cell surface within the culture chamber, calculated by the 3-dimensional model. Linear fit slope: 0.84. Gray line:  $G_m = G_{IN}$ . **(C)** Simulation of the glucose concentration profile at steady-state at the bottom of the culture chamber (top) and in the vertical symmetry plane (bottom) for  $G_{IN}$  equal to 12.7 mM. Flow rate was 0.05  $\mu\text{L}/\text{min}$ .

Next, we performed FRET-based nanosensor experiments to determine cytosolic glucose concentration under different inlet conditions. Flow rate was fixed at approximately 4  $\mu\text{L}/\text{min}$ , high enough for the assumption  $G_m \approx G_{IN}$ , as demonstrated by data in Figure 2C (medium residence time in the chamber was only 11 s).

We applied 4-min pulses of increasing glucose concentrations (0.5-5 mM), separated by 4 min of glucose-free inlet condition (Figure 5A). As expected, the FRET index had larger amplitude of oscillation for pulses of higher glucose concentration. Measurement noise was relevant at low concentrations, but the sensor response showed a good signal-to-noise ratio

for concentrations larger than 1 mM. By approximating FRET response at the end of each pulse as a steady state, first we obtained a nanosensor saturation curve (see Supporting Information) and then derived steady-state cytosolic glucose concentration by Eq. (3) as a function of inlet concentration (Figure 5B). We experimentally found the following linear relationship:

$$G_{\text{cyt}} = 0.12 \cdot G_m \quad (1)$$

that is characteristic of myoblasts stimulated with glucose concentrations up to 5 mM (and maybe even higher), and is independent from the specific experimental setup (system geometry, flow rate).

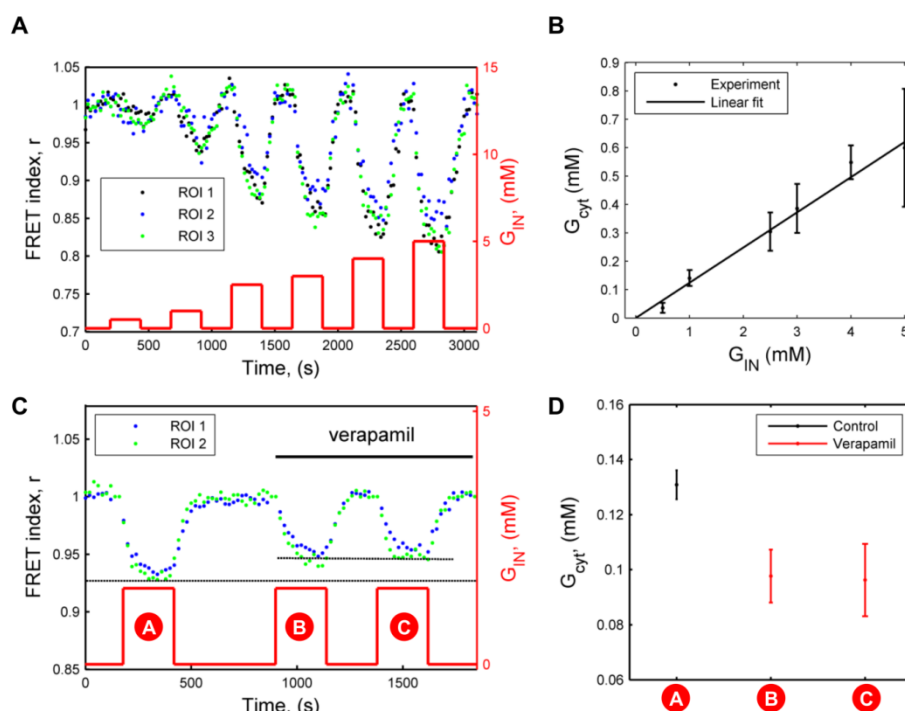


**Figure 5.** Effect of glucose concentration on FRET nanosensor response. (A) Normalized baseline-corrected FRET index,  $r$ , as a function of time during repeated pulses of increasing inlet glucose concentrations (0.5, 1, 2.5, 3, 4, and 5 mM). Black, blue and green dots refer to the signal from 3 different cells. (B) Relationship between steady-state cytosolic and inlet glucose concentrations, derived from data in A. Linear fit slope: 0.12. (C) Effect of verapamil on FRET nanosensor response. Repeated pulses of inlet glucose concentration (1.5 mM), in presence or absence of verapamil (150  $\mu$ M), as indicated. Blue and green dots refer to the signal from 2 different cells. (D) Decrease of steady-state cytosolic glucose concentration, for  $G_{IN} = 1.5$  mM, in presence of the inhibitor ( $p$ -value < 0.05), calculated from the data in C. Flow rate was 4  $\mu$ L/min.

Perturbing the system with the inhibitor verapamil (150  $\mu\text{M}$ ), known to affect glucose transport<sup>24</sup>, we obtained a reduction in cytosolic glucose concentration of about 26%, reducing the constant in (Eq. (1)) to 0.065 (Figure 5C and D). This result is consistent with a 30% decrease in glucose uptake obtained in L929 fibroblasts using radiolabeled 2-deoxyglucose<sup>24</sup>, and shows how impairments can be precisely detected by our system. We also verified the reversibility of this inhibitory mechanism (see Supporting Information).

The linearity of Eq. (1) is confirmed also by the results obtained from a single-cell balance equation at steady state (Eq. (8)). This simple analytical model was developed assuming a first-order intracellular glucose phosphorylation (Eq. (6)), with kinetic constant  $k_g$ . Eq. (8) shows that steady-state  $G_{\text{cyt}}$  is also dependent on another kinetic constant,  $k'_m$ , that characterizes the rate of transport through cell membrane.

As previously mentioned, the steady-state measurements of glucose uptake and cytosolic glucose concentration need to be coupled in order to quantitatively dissect the contribution of the two phenomena of glucose transport through cell membrane and glucose phosphorylation, i.e. to determine  $k'_m$  and  $k_g$ , whose values are reported in Table I. Specifically, Eqs. (8) and (11) were simultaneously solved, the former assuming  $G_m \approx G_{IN}$  and the latter using  $G_m$  from Figure 4B.

The characteristic times (equal to the reciprocal of the kinetic constants) of glucose transport and phosphorylation are 3.7 s and 0.5 s, respectively. Thus, the latter process is 7.4 times faster than the former, making transport the limiting step of glucose handling process, as already well-known.

While hexokinase 1 (HK1) is the main isoform in human skeletal muscle, hexokinase 2 (HK2) is prevalent in mouse<sup>25</sup>. The Michaelis-Menten kinetics of HK2 has been studied in the literature after purification: Michaelis-Menten constant,  $K_m$ , is equal to 0.3 mM and its specific activity to 0.17 U/mg<sup>26</sup>, which corresponds to a  $V_{\text{max}}$  of 0.57 mM/s. When glucose concentration is lower than  $K_m$ , the enzymatic conversion rate can be approximated by a linear expression with proportionality constant  $V_{\text{max}} / K_m$ , equal to 1.9 s<sup>-1</sup>. This value is very close to the  $k_g$  value we obtained experimentally (2.01 s<sup>-1</sup>), however the approximation  $G_{\text{cyt}} \ll K_m$  does not hold for the whole range of  $G_{IN}$  concentrations we used, as shown in Figure 5B.

These results are not contradictory. If in the cellular context the value of  $K_m$  increases, then

the inequality  $G_{\text{cvt}} \ll K_m$  holds and phosphorylation occurs as a 1st-order reaction. To preserve the value of the ratio  $V_{\text{max}} / K_m$ , a parallel increase in  $V_{\text{max}}$  is required. As a speculation, we propose in the Supporting Information an example of a simple dynamics, based on the Briggs-Haldane derivation of the Michaelis-Menten equation, that could support this hypothesis. However, multiple other mechanisms could be equally plausible considering the intracellular molecular crowding.

Our results suggest care in extending *in vitro* kinetics to the cellular context and provide a means to experimentally measure precise metabolic fluxes within the cellular environment. The direct detection of glucose uptake in a microfluidic system offers accuracy at high time resolution and minimal disruption of culture conditions. Furthermore, to the best of our knowledge, we described the first determination of hexokinase phosphorylation rate in living cells under physiological conditions. Our results are particularly relevant in the context of studies on glucose handling processes, involved in the development of dramatic diseases, such as diabetes and cancer, and not restricted to the particular cell system we analyzed.

From a technological point of view, we also investigated the kinetics of the FRET-based nanosensor used in this study, first theoretically and then experimentally. This is particularly important for using the sensor for dynamic real time measurements. In Figure 6A we present the FRET index data shown in Figure 5A, overlapping the results during the first 100 s of each  $G_{\text{IN}}$  pulse. As expected, data show a faster response during cellular uptake at higher glucose concentrations. We fitted each curve by an exponential function to obtain the time constant of the nanosensor,  $\tau$ , which is the same for each curve and equal to 67 s. We confirmed experimentally this result as reported in the Supporting Information. Thus, the binding of glucose to the nanosensor is a very slow process compared to both glucose transport through cell membrane and phosphorylation. As previously mentioned, this means that the FRET-based nanosensor does not give information about the transient cytosolic glucose concentration directly. However, knowing the kinetic constants  $k_m^+$  and  $k_g$ , derived by the procedure above, transient  $G_{\text{cvt}}$  can be calculated mathematically by Eq. (7). Figure 6B shows the results from computational simulations reproducing the experimental conditions of Figure 6A. The dynamics of cytosolic glucose concentration after a change in the intracellular one is much faster than the nanosensor response. This aspect is particularly

relevant and affects the dynamic use of this nanosensor without the combination of other external measurements.

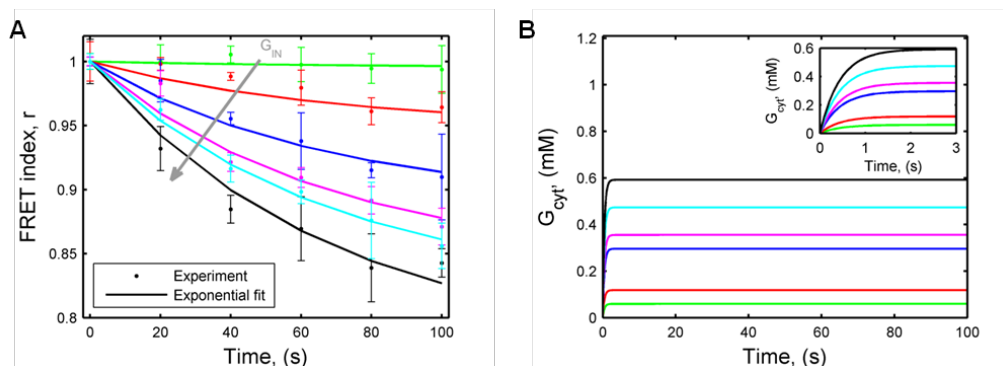


**Figure 6.** Analysis of non-steady-state FRET data. **(A)** Transients of FRET nanosensor response at different inlet glucose concentrations (0.5, 1, 2.5, 3, 4, and 5 mM). Data were derived from experimental results in Figure 5A. Time 0 represents the beginning of pulses at different glucose concentrations. Curves were overlapped and fitted by the exponential function:  $A_i + (1 - A_i) \cdot \exp(-t / \tau)$ , where  $A_i$  ( $i = 1 \dots 6$ ) are constants dependent on  $G_{IN}$  and  $\tau$  is the nanosensor time constant, equal to 67 s. Error bars: standard deviation of 3 ROIs. **(B)** Simulation of cytosolic glucose transient by Eq. (7) under the same conditions of A). An enlargement is shown in the inset.

## Materials and methods

### Single-layer microfluidic chip fabrication

The microfluidic chip containing the cell culture chambers was fabricated according to standard photolithographic techniques<sup>27</sup>. Briefly, the silicon substrate was spin-coated with the negative photoresist SU8-2100 (MicroChem, USA) to obtain a 100- $\mu\text{m}$  thickness of resist layer. After soft baking, UV exposure, post-exposure baking, and development in SU-8 Developer (MicroChem), the mold was hard baked up to 433 K and then cooled to room temperature. Polydimethylsiloxane (PDMS) (Sylgard, Dow Corning, USA) was used for replica molding in the ratio 10:1 (base:cure agent). The mold was treated with chlorotrimethylsilane (Sigma-Aldrich, Italy) vapor for 15 min before casting. The input/output holes on the PDMS chip were made using a 20G needle punch (Small Parts, USA). The PDMS chip was bonded by plasma treatment (Harrick Plasma, USA) onto a 25x60x0.1-mm borosilicate glass cover slip (Menzel Glaser, Germany). Medium reservoirs were built at the inlet and outlet of the chip by adding an additional layer of PDMS.

Specifically, holes were made with a 3-mm diameter Biopsy Punch (Integra LifeSciences, USA) in two 25x10x3-mm PDMS slices, and then bonded by plasma treatment on top of the main chip in correspondence to the input/output holes.

### **Two-layer microfluidic chip fabrication**

The microfluidic chip containing the multi-inlet system required two molds for its fabrication to obtain a two-layer PDMS chip<sup>28</sup>. The former had 25- $\mu$ m round channels (round mold), obtained from SPR 220-7 (Dow Corning) after reflow during the hard bake time. The latter had 25- $\mu$ m square channels (square mold) obtained from SU-8 2025 (MicroChem). PDMS was spun on the square mold to obtain a 50- $\mu$ m thickness layer using a spin coater (Laurell Technologies, USA), and poured on the round mold to make a thick layer (4-5 mm). The thicker PDMS chip was bonded and aligned under a microscope onto the thin one, at the end of the curing phase. The final two-layer chip was bound on a 25x75x1-mm microscope borosilicate glass slide (Menzel Glaser).

### **Myoblast cell line**

C2C12 (ATCC, Italy), an immortalized murine myoblast cell line, were maintained on tissue culture Petri dishes in low-glucose Dulbecco's Modified Eagle Medium (DMEM) (Sigma-Aldrich), supplemented with 10% fetal bovine serum (FBS) (Life Technologies, Italy), and 1% penicillin-streptomycin (pen-strep) solution (Life Technologies). Before confluence, cells were passaged with Trypsin-EDTA 0.05% (Life Technologies) and seeded into the microfluidic chip. Cells were maintained in a humidified incubator at 37°C with 5% CO<sub>2</sub>.

### **Cell culture within the microfluidic chip**

Prior to cell seeding, microfluidic channels and cell culture chambers within the chip were filled with 4°C-cold Matrigel® (Becton-Dickinson, USA) 5% in DMEM, incubated at room temperature for at least 1 hour, and washed with DMEM. A cell suspension was then introduced in the microfluidic chambers in order to obtain a seeding density of 250 cell/mm<sup>2</sup>. After 1-hour incubation at 37°C and 5% CO<sub>2</sub>, culture medium was added drop by drop into the reservoirs to prevent evaporation in the culture chamber and the whole culture system was placed in the incubator. Medium changes were performed every 24 h, by adding fresh medium in the inlet reservoir and aspirating from the outlet using a vacuum pipette. Myoblast differentiation into myotubes occurred spontaneously once myoblasts reached confluence.

## **Immunofluorescence analyses.**

Myoblast differentiation was verified by immunofluorescence analysis for Myosin Heavy Chain II (MHC II), as previously described<sup>29</sup>. Briefly, C2C12 myotubes were fixed with 2% PFA (Sigma-Aldrich) for 7 min, permeabilized with 0.5% Triton X-100 (Sigma-Aldrich) and blocked in 2% horse serum (Life Technologies) for 45 min at room temperature. Mouse monoclonal primary antibody against MHC II (Sigma-Aldrich) was applied for 1 h at 37 °C, followed by incubation with the Alexa488 fluorescence-conjugated anti-mouse IgG secondary antibody (Life Technologies) for 45 min at 37°C. Nuclei were counterstained with Hoechst (Life Technologies) and samples maintained in PBS during fluorescence microscopy analysis.

## **Glucose uptake measurements**

DMEM having 3- to 13-mM glucose concentrations was obtained by mixing 25-mM glucose and glucose-free DMEM media (Life Technologies) in different ratios. DMEM was then supplemented with 10% FBS and 1% pen-strep, and conditioned overnight in the incubator. Using a sterile plastic syringe (Becton-Dickinson), conditioned medium was used to wash four 0.02" ID Tygon® tubes (Cole-Palmer, USA). Each tube was then connected at one end to a 100- $\mu$ L Hamilton syringe (Hamilton, USA) pre-loaded with conditioned medium, and at the other end to the microfluidic chip inlet through a 21G stainless-steel needle (Small Parts). Hamilton syringes were set up on a syringe pump (Harvard Apparatus, USA) and perfusion started at flow rates in the range 0.0125-0.5  $\mu$ L/min. At the outlets of the microfluidic chambers, needles were inserted to facilitate medium collection at different time points. Medium samples of 0.6- $\mu$ L volume were analyzed off-line with FreeStyle Lite® glucometer and strips (Abbott Diabetes Care, Italy) to measure glucose concentration  $G_{OUT}$ .

## **Cell transfections**

Plasmid pcDNA3.1-FLIPglu-600 $\mu$  $\Delta$ 13V, previously developed in our lab<sup>17</sup>, was amplified and purified by GenElute™ HP Plasmid MaxiPrep Kit (Sigma-Aldrich). At the time of transfection, two solutions were prepared: (1) 0.2  $\mu$ g DNA in 25  $\mu$ L Opti-MEM® (Life Technologies), and (2) 1.5  $\mu$ L Lipofectamine in 25  $\mu$ L Opti-MEM. They both were incubated for 5 min at room temperature, mixed together and incubated for another 20 min at room temperature. The final transfection solution was then prepared adding 100  $\mu$ L of Opti-MEM to the previous mixed solution. Part of this transfection solution was used to suspend the

cells to be seeded at a concentration of 5000 cell/ $\mu\text{L}$  into the microfluidic chip. Cells adhered to the surface in about 30 min. The remaining solution was used to change the transfection solution within the chip every hour until the end of transfection (5 h). Then, culture medium was injected into the chip.

### **FRET image acquisition and analysis**

Imaging was performed 24-48 h after transfection at the inverted microscope IX81 (Olympus, Italy) with a 40X/1.30 oil immersion objective (Olympus). The microscope was equipped with a CCD camera (SIS F-View), an illumination system MT20 (Olympus), and a beam-splitter optical device (Multispec Microimager; Optical Insights). Dual emission intensity ratio was simultaneously recorded using cellR 2.0 software (Olympus) after both excitation at 430/25 and 500/20 for the two emission filters (470/30 CFP and 535/30 for YFP). Images were acquired within the linear detection range of the camera at intervals of 20 s for up to 1 hour. Exposure time was set to 200 ms. All experiments were carried out at room temperature.

Acquired FRET images were analyzed as previously reported<sup>17</sup>, with spectral bleed-through (SBT) and baseline correction using polynomial fit. The analysis produced the normalized baseline-corrected FRET index,  $r$ .

### **FRET experiments**

During FRET image acquisition, perfusion through the cell culture chamber was performed at 4  $\mu\text{L}/\text{min}$ . Cells were imaged in DPBS with calcium and magnesium 1X (Life Technologies) with added different glucose concentrations (Sigma-Aldrich). A microfluidic multi-inlet system was placed upstream of the culture chamber and connected by a vertical 5-cm long PEEK tube, having inner diameter of 65  $\mu\text{m}$  (IDEX, USA), to produce the pressure-driven flow. This system allowed switching between up to 9 different glucose concentrations during an experiment by controlling valve opening and closing via LabView software (National Instruments, Italy). Cyclic pulses of different glucose concentrations were alternated with glucose-free infusion every 4 min.

### **Determination of cytosolic glucose concentration**

The normalized baseline-corrected FRET index,  $r$ , was used to calculate glucose saturation,  $S$ , of FRET nanosensor by the following expression:

$$S = 1 - \frac{r - r_{\min}}{r_{\max} - r_{\min}}, \quad (2)$$

where  $r_{\min}$  represents FRET index under glucose-free conditions, and  $r_{\max}$  the index under high glucose concentrations at sensor saturation. Steady-state cytosolic glucose concentration,  $G_{\text{cyt},ss}$ , is then obtained using the glucose dissociation constant,  $K_d$ , equal to 0.59 mM from previous nanosensor calibration<sup>17</sup>:

$$G_{\text{cyt},ss} = \frac{K_d \cdot S}{1 - S}. \quad (3)$$

### Three-dimensional mathematical model

A 3D mathematical model was developed to describe fluid dynamics and mass transport in the experimental system. The system geometry included the cell culture chamber and the inlet and outlet microfluidic channels. Geometric dimensions matched those of the experimental setup. Because of the system symmetrical geometry, only one half of it was simulated. The velocity field in the microfluidic channel was obtained solving the continuity equation and the equation of motion for an incompressible Newtonian fluid. The glucose concentration field was obtained by solving its equation of continuity. Glucose uptake by the cell layer at the bottom of the culture chamber was included in the model as a flux boundary condition, i.e. by an outward homogeneous glucose flux proportional to glucose concentration on the surface. The proportionality constant,  $k_v$ , was obtained by least-square regression of glucose uptake measurements and equal to  $3 \cdot 10^{-8}$  m/s. The mean value of medium concentration in the vicinity of the cells,  $G_m$ , was calculated by numerical integration of glucose concentration on the bottom surface of cell culture chamber. The model was implemented in Comsol Multiphysics (COMSOL, Sweden) using a relative tolerance of  $10^{-6}$  for the solution. Coarsening and refining the mesh space grid ensured that the results were independent of the spatial discretization.

### Single-cell model

An analytical model was also developed in the form of a single-cell balance equation, including the flow of glucose across the cell membrane,  $F_m$ , and that of glucose intracellular consumption through glycolysis,  $F_g$ :

$$V_c \frac{dG_{\text{cyt}}}{dt} = F_m - F_g, \quad (4)$$

where  $G_{cvt}$  represents glucose concentration in the cytoplasm,  $t$  is time, and  $V_c$  represents the intracellular volume where glucose is phosphorylated. We assumed  $V_c$  equal to the cytosolic volume, as studies on hexokinase exclude a nuclear localization for this enzyme under normal conditions<sup>18,30</sup>. At steady-state, the term on the left hand side of (4) is null.

The first flow rate on the right hand side is expressed as:

$$F_m = k_m \cdot S_c \cdot (G_m - G_{cvt}), \quad (5)$$

where  $k_m$  is the overall mass transfer coefficient and  $S_c$  represents the cell surface. The second flow rate, due to glucose phosphorylation by hexokinase enzyme, is given by the following expression:

$$F_g = k_g \cdot V_c \cdot G_{cvt}, \quad (6)$$

where  $k_g$  is the reaction kinetic constant.

After substitution of Eqs. (5) and (6), cytosolic glucose concentration,  $G_{cvt}$ , after a step change from 0 to  $G_{IN}$ , is obtained by Eq. (4):

$$G_{cvt}(t) = \frac{k_m'}{k_m' + k_g} \cdot (1 - \exp(-(k_m' + k_g) \cdot t)) \cdot G_{IN}, \quad (7)$$

where  $k_m' = k_m \cdot S_c / V_c$ ; and steady-state glucose concentration,  $G_{cvt,ss}$ , is then:

$$G_{cvt,ss} = \frac{k_m'}{k_m' + k_g} \cdot G_m. \quad (8)$$

## Overall mass balance

A macroscopic mass balance was performed considering the whole culture chamber as the system of interest. The overall glucose uptake,  $U$ , by the cell population is given by the following expression:

$$U = \dot{V} \cdot (G_{IN} - G_{OUT}), \quad (9)$$

where  $\dot{V}$  is medium flow rate,  $G_{IN}$  and  $G_{OUT}$  are glucose concentrations at the inlet and outlet of the chamber, respectively. At steady state, flow rates are equals and these equalities hold:

$$U = N_c \cdot F_m = N_c \cdot F_g, \quad (10)$$

where  $N_c$  represents the number of cells in the culture chamber. Combining Eqs. (5), (6) and (10), the following expression is obtained:

$$U = \left( \frac{1}{k_m} + \frac{1}{k_g} \right)^{-1} \cdot N_c \cdot V_c \cdot G_m. \quad (11)$$

## Conclusions

We developed a methodology for quantitatively dissecting the kinetics of glucose intracellular transport, single-cell uptake and phosphorylation kinetics in live myoblasts. We took advantage of multiple technologies: a microfluidic system that enhances cell microenvironment dynamic control and measurement sensitivity, a FRET-based nanosensor that measures cytosolic glucose in live cells with high spatial resolution, and mathematical modeling to assist data interpretation.

We used this procedure to analyze glucose metabolism in myoblasts, accurately determining single-cell kinetics of glucose flow through cell membrane and phosphorylation. In particular, we found the following results in myoblasts under physiological glucose concentrations: (1) steady-state cytosolic glucose concentration is only 12% of the intracellular concentration in the immediate vicinity of cell membrane; (2) intracellular glucose phosphorylation is 7.4 times faster than glucose transport through cell membrane; (3) the characteristic times of transport and phosphorylation are 3.7 s and 0.5 s, respectively; (4) the time required for a cell to reach a new steady state after a change in extracellular glucose concentration is approximately 2 s; (5) within the intracellular context hexokinase has a 1st-order kinetics also at higher glucose concentrations compared to what was previously known from studies performed with the purified enzyme.

We also found that FRET-based nanosensor FLIPglu-600 $\mu\Delta$ 13V can be used for dynamic cytosolic measurements only indirectly via mathematical modeling, as its kinetics is much slower than those of cellular glucose handling processes. However, through mathematical modeling, it can be successfully used for very accurate measurements of intracellular kinetics under physiological conditions, once its measurement is coupled with the detection of glucose uptake.

A very relevant perspective of this work is the extension of glucose-related processes dissection to different biological systems involved in metabolic impairments. In particular, live myotubes are phenotypically more similar to skeletal muscle *in vivo*, compared to myoblasts. We were able to efficiently differentiate myoblasts within the microfluidic culture chamber, obtaining myotubes showing a mature sarcomeric organization (Figure 7).

Currently, direct transfection of myotubes with the FRET nanosensor resulted too inefficient for reliable measurements. However, transfecting them using a different vector for constitutive expression, such as a lentivirus encoding the nanosensor, could overcome this limitation and extend the applicability of the methodology.

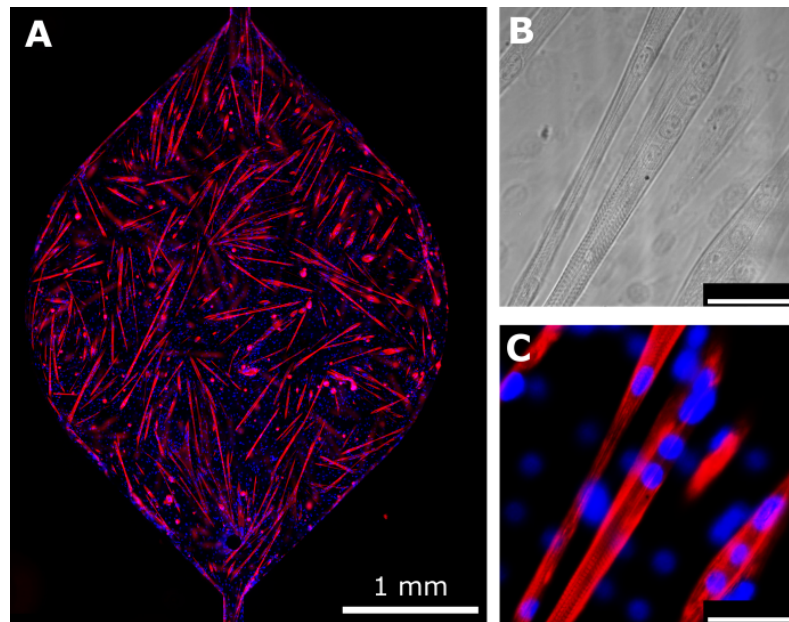


**Figure 7.** Differentiated myotubes within the microfluidic culture chamber. (A) Immunofluorescence analysis of myotubes derived from murine myoblasts after 7 days of differentiation. Red: myosin heavy chain II, blue: Hoechst for nuclei. (B-C) Enlargement of myotubes in (A), bright field and fluorescence images highlighting the sarcomeric structure. Scale bar: 50  $\mu\text{m}$ .

## Acknowledgement

This work was supported by Progetti di Eccellenza CaRiPaRo and the European Foundation for the Study of Diabetes, WBF was supported by funds from the Carnegie Institution.

## Notes and references

Electronic Supplementary Information (ESI) available

1. B. M. Frier, *Diabetologia*, 2009, **52**, 31–34.

2. M. Laakso, *Diabetes*, 1999, **48**, 937–942.
3. P. E. Cryer, S. N. Davis, and H. Shamon, *Diabetes Care*, 2003, **26**, 1902–1912.
4. A. P. Rolo and C. M. Palmeira, *Toxicol. Appl. Pharmacol.*, 2006, **212**, 167–178.
5. J. Kim and C. V. Dang, *Cancer Res.*, 2006, **66**, 8927–8930.
6. R. B. Bird, W. E. Stewart, and E. N. Lightfoot, *Transport Phenomena*, John Wiley & Sons, 2007.
7. B. Thorens and M. Mueckler, *Am. J. Physiol. - Endocrinol. Metab.*, 2010, **298**, E141–E145.
8. K. Ohtsubo, M. Z. Chen, J. M. Olefsky, and J. D. Marth, *Nat. Med.*, 2011, **17**, 1067–1075.
9. C. Luni, J. D. Marth, and F. J. Doyle, *PLoS ONE*, 2012, **7**, e53130.
10. L. Sokoloff, M. Reivich, C. Kennedy, M. H. D. Rosiers, C. S. Patlak, K. D. Pettigrew, O. Sakurada, and M. Shinohara, *J. Neurochem.*, 1977, **28**, 897–916.
11. F. Turkheimer, R. M. Moresco, G. Lucignani, L. Sokoloff, F. Fazio, and K. Schmidt, *J. Cereb. Blood Flow Metab.*, 1994, **14**, 406–422.
12. W. H. Kim, J. Lee, D.-W. Jung, and D. R. Williams, *Sensors*, 2012, **12**, 5005–5027.
13. L. Speizer, R. Haugland, and H. Kutchai, *Biochim. Biophys. Acta BBA - Biomembr.*, 1985, **815**, 75–84.
14. K. Yoshioka, H. Takahashi, T. Homma, M. Saito, K.-B. Oh, Y. Nemoto, and H. Matsuoka, *Biochim. Biophys. Acta BBA - Gen. Subj.*, 1996, **1289**, 5–9.
15. M. Kurtoglu, J. C. Maher, and T. J. Lampidis, *Antioxid. Redox Signal.*, 2007, **9**, 1383–1390.
16. M. Fehr, S. Lalonde, I. Lager, M. W. Wolff, and W. B. Frommer, *J. Biol. Chem.*, 2003, **278**, 19127–19133.
17. B.-H. Hou, H. Takanaga, G. Grossmann, L.-Q. Chen, X.-Q. Qu, A. M. Jones, S. Lalonde, O. Schweissgut, W. Wiechert, and W. B. Frommer, *Nat. Protoc.*, 2011, **6**, 1818–1833.
18. J. E. Wilson, *J. Exp. Biol.*, 2003, **206**, 2049–2057.
19. J. D. Lueck and H. J. Fromm, *J. Biol. Chem.*, 1974, **249**, 1341–1347.
20. W. T. Jenkins and C. C. Thompson, *Anal. Biochem.*, 1989, **177**, 396–401.
21. S. Rodríguez-Enríquez, A. Marín-Hernández, J. C. Gallardo-Pérez, and R. Moreno-Sánchez, *J. Cell. Physiol.*, 2009, **221**, 552–559.
22. C. X. Bittner, A. Loaiza, I. Ruminot, V. Larenas, T. Sotelo-Hitschfeld, R. Gutiérrez, A. Córdova, R. Valdebenito, W. B. Frommer, and L. F. Barros, *Front. Neuroenergetics*, 2010, **2**, 26.
23. N. Kotliar and P. F. Pilch, *Mol. Endocrinol.*, 1992, **6**, 337–345.
24. L. L. Louters, N. Stehouwer, J. Rekman, A. Tidball, A. Cok, and C. P. Holstege, *J. Med.*

*Toxicol.*, 2010, **6**, 100–105.

25. J. E. Wilson, in *Reviews of Physiology, Biochemistry and Pharmacology, Volume 126*, Springer Berlin Heidelberg, Berlin, Heidelberg, 1995, vol. 126, pp. 65–198.

26. R. L. Printz, S. Koch, L. R. Potter, R. M. O’Doherty, J. J. Tiesinga, S. Moritz, and D. K. Granner, *J. Biol. Chem.*, 1993, **268**, 5209–5219.

27. J. C. McDonald and G. M. Whitesides, *Acc. Chem. Res.*, 2002, **35**, 491–499.

28. J. Melin and S. R. Quake, *Annu. Rev. Biophys. Biomol. Struct.*, 2007, **36**, 213–231.

29. S. Zatti, A. Zoso, E. Serena, C. Luni, E. Cimetta, and N. Elvassore, *Langmuir ACS J. Surf. Colloids*, 2012, **28**, 2718–2726.

30. S. John, J. N. Weiss and B. Ribalet, *PLoS One*, 2011,6(3), e17674.

## Electronic Supplementary Information (ESI)

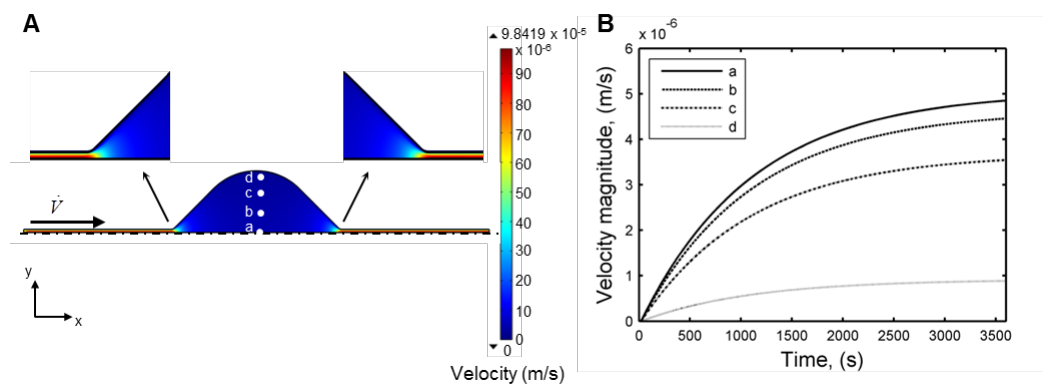


**Figure S1.** Fluid dynamics study using the developed 3D model. (A) Simulation of the velocity field at steady state in the median plane ( $z = H/2$ ) of the culture chamber. Flow rate was  $0.05 \mu\text{L}/\text{min}$ . (B) Velocity magnitude during the step change in flow rate from 0 to  $0.05 \mu\text{L}/\text{min}$ . a, b, c, and d, refer to the positions indicated in A).

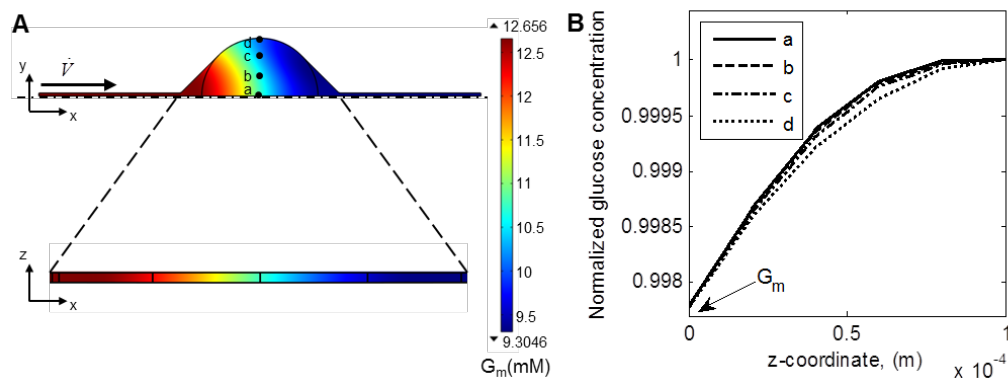


**Figure S2.** Study of the concentration profile within the microfluidic chip simulated by the developed 3D model. (A) Same as Figure 4C, with indicated the position of points a, b, c, d plotted in B). (B) Glucose concentration along the z-direction at positions indicated in A). Concentration was normalized by the concentration at the top of the channel ( $z = H$ ) in each position.

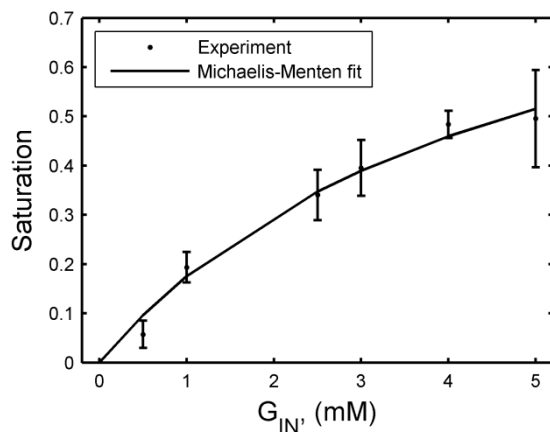
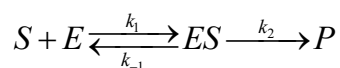


**Figure S3.** FRET-based nanosensor saturation curve. Saturation was calculated by Eq. (2) from the steady-state FRET data presented in Figure 5A. Solid line represents the results of least-square data fitting by a Michaelis-Menten-like equation.

## Potential hexokinase enzymatic rate modification in the intracellular environment

We considered the classical elementary steps of an enzymatic reaction:



where  $S$  represents glucose,  $E$  hexokinase enzyme,  $ES$  the enzyme-substrate complex, and  $P$  glucose-6-phosphate. Mass-action kinetic parameters are indicated as  $k_1$ ,  $k_{-1}$ , and  $k_2$ .

The Briggs-Haldane derivation of Michaelis-Menten equation assumes  $ES$  concentration is at quasi-steady state, i.e. in mathematical terms:

$$k_1 [E][S] \approx (k_{-1} + k_2)[ES] \quad (\text{S12})$$

where square brackets represent concentrations. Following this approximation the well-known Michaelis-Menten equation is obtained:

$$\frac{d[P]}{dt} = \frac{V_{\max} [S]}{K_m + [S]}, \quad (\text{S13})$$

where the values of parameters  $K_m$  and  $V_{\max}$  are related to the mass-action constants by the following expressions:

$$K_m = \frac{k_{-1} + k_2}{k_1}, \quad (\text{S14})$$

and

$$V_{\max} = k_2 [E]_0, \quad (\text{S15})$$

where  $[E]_0$  is the total (constant) enzyme concentration in its bound and unbound states.

From Eqs. (S14) and (S15), the ratio of  $V_{\max}$  to  $K_m$  is given by the following relationship:

$$\frac{V_{\max}}{K_m} = \frac{k_2 [E]_0}{\frac{k_{-1} + k_2}{k_1}}. \quad (\text{S16})$$

Under the feasible assumption that  $k_{-1} \ll k_2$ , Eq. (S16) becomes:

$$\frac{V_{\max}}{K_m} \approx \frac{k_2 [E]_0}{\frac{k_2}{k_1}} = k_1 [E]_0. \quad (\text{S17})$$

Eq. (S17) shows that under the two simple assumptions above, it is possible to have a linear relationship between  $V_{\max}$  and  $K_m$ . Assuming that, compared to *in vitro* enzymatic experiments, the intracellular environment favors the production of glucose-6-phosphate by speeding up the reaction described by parameter  $k_2$ , this would imply an increase in  $V_{\max}$  and  $K_m$ , without affecting their ratio.

## **Analysis of FRET-based nanosensor characteristic time**

We performed further experiments using the FRET-based nanosensor to verify the accuracy of its time constant that we obtained. In particular, we stimulated the cells with approximately linear ramps of glucose concentration at increasing rate (Figure S4 A).

According to the model developed, once the rise in glucose concentration is faster than the rate of nanosensor response, the nanosensor responds at its maximum rate and its half-time for saturation ( $t_{1/2}$ ) is not affected by a further increase in the speed of the ramp any more (Figure S4 B).

The experimental results we obtained confirm this theoretical prediction. In particular, Figure S4 F shows that experimental results are in agreement with model simulations. Below about 10<sup>0</sup> min, the nanosensor characteristic time, the half-time for saturation remains approximately constant.

One would say that other resistances could be present that prevent nanosensor access to glucose as it is intracellular. However, we obtained the characteristic time of glucose uptake by myoblasts in culture, equal to 3.7 s, through repeated enzymatic assays of medium out flowing from the culture chamber, in a microfluidic culture system that enhanced the signal-to-noise-ratio. As the process of glucose transport through cell membrane is much faster than the interaction of glucose with the nanosensor, it is possible to analyze the kinetics of the nanosensor within the cell, because the cell membrane transport is essentially not affecting the measurement.

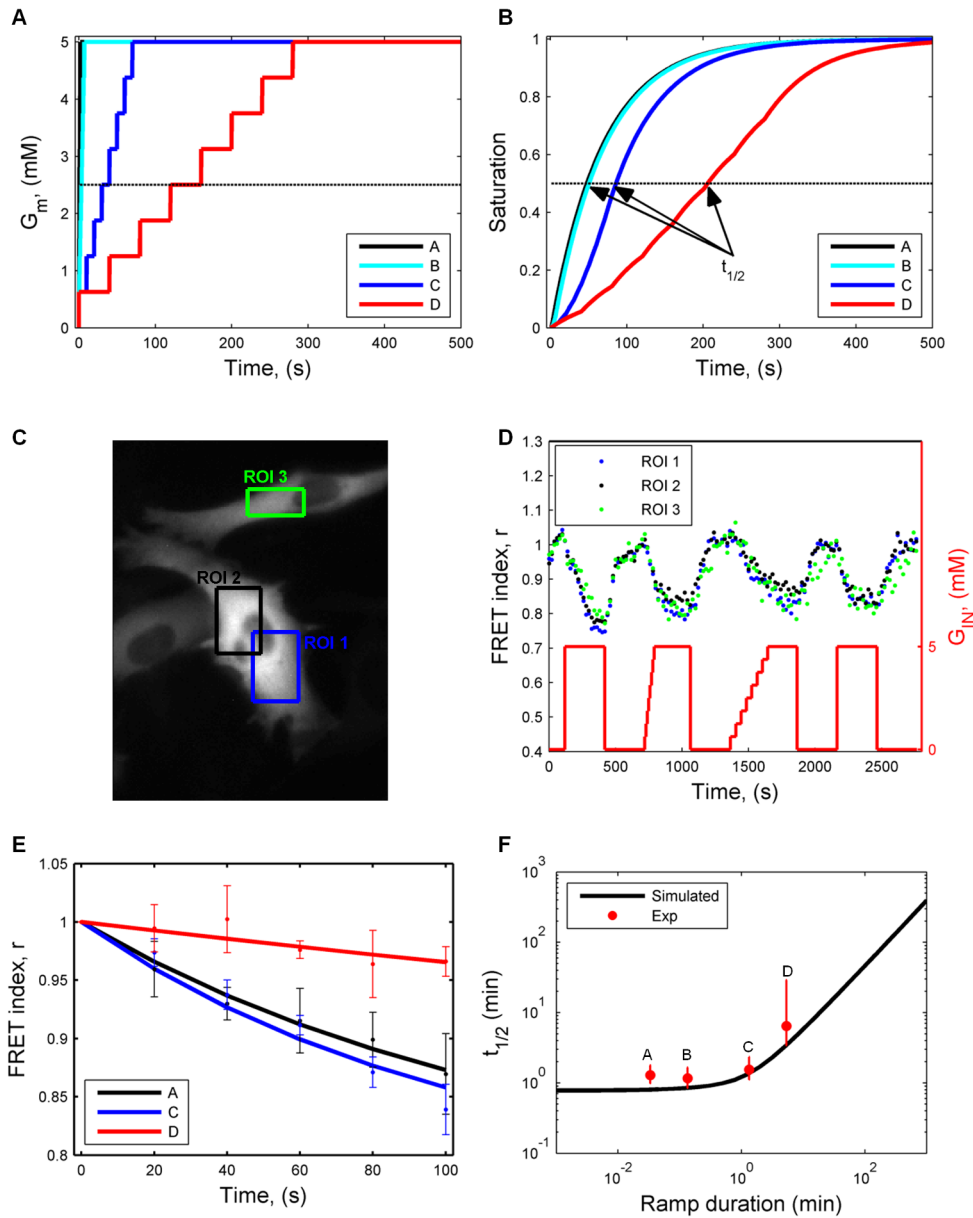


**Figure S4.** Study of FRET-based nanosensor time constant. **(A)** Simulated approximately linear ramps of glucose concentration of increasing rate. The step approximation mimics the inflow from the multi-inlet system into the culture chamber. **(B)** Model predictions of the nanosensor response to the stimuli described in **(A)**. **(C)** Image of YFP fluorescence and indication of the ROIs analyzed in **(D)** and **(E)**. **(D)** Experimental data of FRET-based nanosensor response to the glucose concentration profile indicated. **(E)** Analysis of the transient of FRET index decay following an increase in glucose concentration as shown in **(D)**. Error bars indicate the standard deviation calculated from the 3 ROIs. **(F)** Comparison between the half-time for sensor saturation obtained by experimental data and model simulations. The experiment was repeated twice.

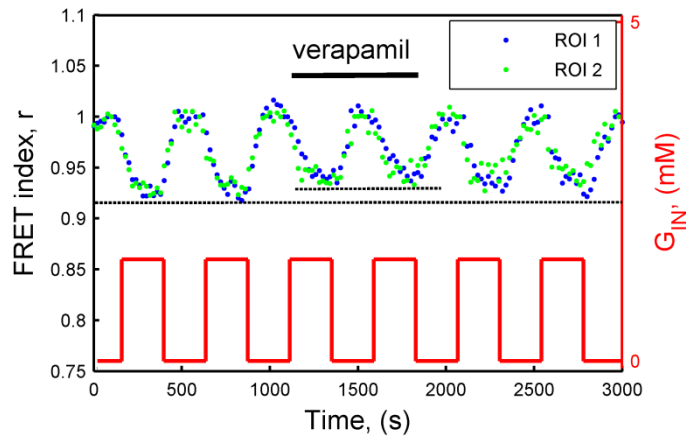


**Figure S5.** Effect of verapamil stimulation on cell response to glucose. Normalized baseline-corrected FRET index,  $r$ , as a function of time during repeated pulses of 1.5-mM glucose concentration, in presence or absence of glucose transport inhibitor, verapamil (150  $\mu$ M). Removal of verapamil after 2 glucose pulses shows the inhibitory effect is reversible. Blue and green dots refer to the signal from 2 different cells. Flow rate was 4  $\mu$ L/min.